

DOI: 10.1002/chem.201700203

Full Paper

## Synthesis of Hexagonal FeMnP Thin Films from a Single-Source Molecular Precursor

**Andrew<sup>^</sup>P. Leitner,<sup>[a]</sup> Desmond<sup>^</sup>E. Schipper,<sup>[a]</sup> Jing Han Chen,<sup>[a]</sup> Adam<sup>^</sup>C. Colson,<sup>[a]</sup> Irene Rusakova,<sup>\*[b]</sup> Binod<sup>^</sup>Kumar Rai,<sup>[c]</sup> Emilia Morosan,<sup>\*[a,c]</sup> and Kenton<sup>^</sup>H. Whitmire<sup>0000-0001-7362-535X</sup><sup>\*[a]</sup>**

<sup>[a]</sup> <orgDiv/>Department of Chemistry  
<orgName/>Rice University, MS 60  
<street/>6100 Main Street  
<city/>Houston, <countryPart/>Texas <postCode/>77005-1892 (<country/>USA)  
E-mail: whitmir@rice.edu  
E-mail: emorosan@rice.edu

<sup>[b]</sup> <orgDiv/>Texas Center for Superconductivity  
<orgName/>University of Houston  
<street/>202 UH Science Center  
<city/>Houston, <countryPart/>Texas <postCode/>77204-5002 (<country/>USA)  
E-mail: rusakova@uh.edu

<sup>[c]</sup> <orgDiv/>Department of Physics and Astronomy  
<orgName/>Rice University, MS 61  
<street/>6100 Main Street  
<city/>Houston, <countryPart/>Texas <postCode/>77005-1892 (<country/>USA)

<pictid> Supporting information and the ORCID identification number(s) for the author(s) of this article can be found under:

<+><url><http://dx.doi.org/10.1002/chem.201700203></url>.

**Thin film:** Ternary bimetallic thin films of the hexagonal, metastable phase of FeMnP are grown from a single-source precursor, FeMn(CO)<sub>9</sub>( $\mu$ -PH<sub>2</sub>), on different substrates at low

temperatures through metal-organic chemical vapor deposition (MOCVD). The magnetic properties of this material are measured for the first time and compared to theoretical values.

Whitmire et al. @RiceUniversity @UHouston on thin films of FeMnP and their

#magneticproperties

---

## Magnetic Properties

---

magnetic materials

magnetic properties

pnictides

supported catalysts

thin films

transition metals

The first heterobimetallic phosphide thin film containing iron, manganese, and phosphorus, derived from the single-source precursor  $\text{FeMn}(\text{CO})_8(\mu\text{-PH}_2)$ , has been prepared using a home-built metal-organic chemical vapor deposition apparatus. The thin film contains the same ratio of iron, manganese, and phosphorus as the initial precursor. The film becomes oxidized when deposited on a quartz substrate, whereas the film deposited on an alumina substrate provides a more homogeneous product. Powder X-ray diffraction confirms the formation of a metastable, hexagonal FeMnP phase that was previously only observed at temperatures above  $1200^\circ\text{C}$ . Selected area electron diffraction on single crystals isolated from the films was indexed to the hexagonal phase. The effective moment of the films ( $\mu_{\text{eff}}=3.68\mu_{\text{B}}$ ) matches the previously reported theoretical value for the metastable hexagonal phase, whereas the more stable orthorhombic phase is known to be antiferromagnetic. These results not only demonstrate the successful synthesis of a bimetallic, ternary thin film from a single-source precursor, but also the first low temperature approach to the hexagonal phase of FeMnP.

## Introduction

The metal pnictides are a family of materials composed of transition metals and group 15 elements, and bulk metal pnictides have been studied extensively for at least fifty years

due to the applicability of their physical and chemical properties.<sup>[1--4]</sup> Bulk transition metal phosphides (TMPs) have garnered recent attention due to their ability to catalyze the hydrogen evolution reaction (HER) and oxygen evolution reaction (OER).<sup>[5,^6]</sup> Binary and ternary TMP nanoparticles and thin films have shown excellent performance for catalyzing the HER and OER<sup>[7--17]</sup> owing to their higher surface areas as well as deviations from the properties of the bulk materials at the nanoscale.<sup>[18--24]</sup> In some cases the bimetallic alloys are predicted to perform better than their single metal counterparts.<sup>[25]</sup>

Metal pnictide nanoparticles may be synthesized by thermally decomposing organometallic precursors in the presence of reactive pnictide species of the form  $ER_3$  (E=P or As, R=H, alkyl, aryl, or silyl). The nanoparticle reactions are usually carried out in a high-boiling solvent in the presence of stabilizing additives.<sup>[18,^26--30]</sup> The significant progress achieved by employing these methods notwithstanding, there are several difficulties associated with solution-based metal syntheses of advanced metal pnictides. The stoichiometric composition of the nanoparticles can be difficult to control, particularly if one of the precursors is used in excess or if the precursors have substantially different thermal stabilities or decomposition rates. This is especially problematic for the transition metal pnictides where a wide range of possible stoichiometries exist. For example, with  $Fe_xP_y$  both metal rich phases ( $y=1, x=1--4$ ) and phosphorus rich phases ( $x=1, y=1, 2, \text{ and } 4$  are known). Additionally, the composition of the nanoparticles can be affected by non-innocent interactions between the particles and solvents or stabilizing agents in solution. Recently, our group prepared iron-rich  $Fe_{2<M>x}Mn_xP$  nanoparticles using the single-source molecular precursor  $FeMn(CO)_8(\mu-PH_2)^{[31]}$  but the nanoparticles were found to be manganese poor due to leaching of that metal by oleic acid.

Synthesizing the metal pnictide materials through metal-organic chemical vapor deposition (MOCVD) can eliminate the possibility of unfavorable interactions between the desired metal pnictide material and solvents or stabilizing agents. The MOCVD technique has been successfully employed in the preparation of a number of binary TMP films.<sup>[21,^32--46]</sup> We have reported the preparation of phase-pure ferromagnetic binary  $Fe_3P$  films using the single-source molecular precursor  $H_2Fe_3(CO)_9PR$  (R=*t*Bu) deposited in a rudimentary MOCVD

apparatus.<sup>[47]</sup> Moreover, we also established a route to ternary phase TMPs by simultaneously decomposing multiple molecular precursors onto a quartz substrate to produce Fe<sub>3</sub>P films doped with cobalt and tellurium.<sup>[48]</sup>

A feasible method of preparing ternary, bimetallic thin films from a single source precursor has not yet been reported. This paper reports the use of FeMn(CO)<sub>8</sub>( $\mu$ -PH<sub>2</sub>) as the ideal single-source precursor for the production of thin films of FeMnP. For thin films grown on quartz, the X-ray photoelectron spectroscopy (XPS) measurements suggest the manganese was preferentially oxidized near the quartz interface and an inconsistent stoichiometry for iron, manganese and phosphorus was observed. We resolved this oxidation issue by replacing the substrates with alumina, which has a lower Gibbs free energy than quartz. The nanoscale crystallites of the resulting films were elucidated by scanning electron microscopy (SEM) and planar defects observed in the high resolution transmission electron microscopy (HRTEM), while the hexagonal phase was confirmed by single-crystal selected area electron diffraction (SAED).

The hexagonal phase of FeMnP has only previously been observed above 1200<sup>o</sup>C and reverted to the orthorhombic phase upon cooling, preventing any subsequent characterization.<sup>[49]</sup> The magnetic significance of compounds crystallizing in the hexagonal Fe<sub>2</sub>P-type structure ( $P6\bar{3}m$ ) has been established.<sup>[50-54]</sup> For the first time, the magnetic properties of this metastable phase of FeMnP were measured with a magnetic property measurement system (MPMS) and are consistent with the theoretical values.<sup>[55]</sup>

## Experimental Section

### General considerations

The organometallic cluster FeMn(CO)<sub>8</sub>( $\mu$ -PH<sub>2</sub>) was prepared according to the previously described methods.<sup>[56]</sup> The precursor was stored under inert gas to avoid oxidation and decomposition. The substrates were washed with acetone and dried under vacuum before deposition. All films were kept under argon or nitrogen before and after all instrumental characterizations to prevent additional oxidation or adsorption of atmospheric contaminants.

### Thin film depositions

The previously described MOCVD apparatus that was used for the synthesis of Fe<sub>3</sub>P was used for all depositions and a schematic of the device is shown in Figure<sup>1</sup>.<sup>[47]</sup> The MOCVD apparatus employed in this work consists of a quartz tube, of inner diameter 22 mm, equipped with a Kimble--Chase high vacuum valve at the end furthest from the precursor and capped with a size 25 o-ring joint/cap assembly. All loading and unloading of the apparatus took place in a nitrogen atmosphere glove box. 15 mm<sup>2</sup> substrates (quartz or alumina) were affixed to the stainless steel heating stage with silver paste and heated at 130°C in air to cure the silver paste and provide good thermal contact. The single source precursor (15 mg of FeMn(CO)<sub>8</sub>(μ-PH<sub>2</sub>)) was transferred to a glove box under a nitrogen atmosphere, and into the end of the tube apparatus, followed by the substrate-affixed heating stage, and the tube was subsequently sealed. The apparatus was transferred to a high-vacuum manifold and the end of the apparatus with the precursor was submerged in a liquid nitrogen bath. While the precursor was kept at 77 K, the apparatus was evacuated until a cold-cathode ionization vacuum gauge stabilized at approximately  $2 \times 10^{-6}$  torr. The position of the heating stage in the apparatus was adjusted to achieve optimum substrate coverage (Figure<sup>1</sup>). Zone 1 of the apparatus, where the substrates were located, was then heated to 350°C for 30 minutes by wrapping with heating tape connected to a variac. The nitrogen bath was removed from the precursor and the precursors was allowed to warm to room temperature. After 20 minutes, a metallic film had formed on the substrates and walls surrounding the substrate assembly. The apparatus was disassembled under nitrogen and the material stored in a glove box.

### Film characterizations

Quantitative elemental analyses of iron, manganese, and phosphorus were carried out by inductively coupled plasma optical emission spectroscopy (ICP-OES) with an internal yttrium standard. The films were digested in concentrated nitric acid with sonication, followed by dilution to a suitable concentration with trace-metal-free nitric acid and water. The spectral emission lines at 259.939, 294.920, and 214.914 nm were selected for analysis of iron, manganese, and phosphorus, respectively. Iron and manganese were analyzed by radial plasma viewing, while phosphorus was analyzed by axial plasma viewing.

X-Ray photoelectron spectroscopy (XPS) was carried out on a Physical Electronics PHI Quantera SXM instrument using a monochromatic AlK<sub>α</sub> source (1486.6 eV) operated at 40.7 W with

a beam size of 200 $\mu\text{m}$  and a take-off angle of 45°. A band pass of 69 $\text{eV}$  was used for the accurate determination of the iron 2p<sub>3/2</sub>, manganese 2p<sub>3/2</sub>, oxygen 1s, and phosphorus 2p binding energies (BE's) and their relative concentrations. The films were sputtered with an Ar<sup>+</sup> ion beam (3 $\text{keV}$ ) for 3--5 minutes prior to analysis to remove any surface oxidation or contaminants. A 3 $\text{keV}$  Ar<sup>+</sup> ion beam was used on a 2 $\times$ 2 $\text{mm}$  area on the films for all sputtering during depth profile studies. The peak positions were calibrated using the 1s peak from adventitious carbon (284.8 $\text{eV}$ ).

Scanning electron microscopy (SEM) was carried out on a FEI Quanta 400 FEG microscope operated in secondary electron mode at 30 $\text{kV}$ . SEM images were obtained on the native films; it was not necessary to sputter-coat the films prior to imaging due as they were suitably conductive. The film thicknesses were determined by analyzing the cross-section of selected films.

Powder X-ray diffraction (PXRD) data were collected on a Rigaku D/Max-2100PC powder diffractometer using unfiltered Cu $\text{K}\alpha$  radiation at 40 $\text{kV}$  and 40 $\text{mA}$ , a step size of 0.05 $^\circ 2\theta$ , and a scan rate of 0.5 $^\circ 2\theta \text{min}^{-1}$ . Rietveld refinements performed with the GSAS software are shown in the Supporting Information.

Transmission electron microscopy (TEM) was carried out using FEI G2, JEOL 2000 FX, and JEM 2010F microscopes, equipped with energy dispersive spectrometers, operated at 200 $\text{kV}$ . Conventional and HRTEM imaging, selected area electron diffraction (SAED), and EDX spectroscopy, including elemental mapping methods, were used for analysis of the nanoparticles. All TEM samples were deposited on 300 $\mu\text{m}$  mesh holey-carbon-coated copper grids.

Magnetic measurements were carried out using a Quantum Design Magnetic Property Measurement System (MPMS) on the thin films deposited on aluminum slides as well as the material that flaked off of the quartz walls of the MOCVD apparatus. The materials were packed with TaegaSeal PTFE Tape in the measurement straw holder, assuring that the diamagnetic contribution due to the tape was negligible compared to the signal of the samples.

## Results and Discussion

### Composition of films

The molecular species FeMn(CO)<sub>8</sub>( $\mu$ -PH<sub>2</sub>) is the ideal single-source precursor to thin films of FeMnP. An MOCVD apparatus, with an independently controlled two-zone heating

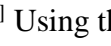
system, was used to volatilize and decompose the organometallic precursor to produce films with a metallic appearance on the substrates attached to the heating stage. The elemental ratios, measured by ICP-OES, for the deposited films showed iron, manganese, and phosphorus to be in a 1:1:1 ratio; the Fe:Mn:P stoichiometry of the precursor being conserved in the films.

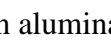
Depth profiling through XPS was carried out on the thin films in order to assess the elemental composition and homogeneity of the deposited material. The depth profile of the films deposited on quartz indicated that the atomic percentages of iron, manganese, and phosphorus were not constant throughout the thickness of the film (Figure<sup>2</sup>(a)). While the films showed an Fe:Mn:P stoichiometric ratio of 1.3:0.8:1 near the surface, the oxygen and manganese amount increased towards the interface with the quartz substrate indicating a reaction between the film and quartz substrate. This selective oxidation of manganese by quartz substrates in bimetallic systems has been observed in the supported catalyst Co-Mn/SiO<sub>2</sub>.<sup>[57]</sup>

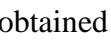
In order to minimize the oxidation of the film by the substrate, alumina substrates were explored because Al<sub>2</sub>O<sub>3</sub> is much less reactive due to its low Gibbs free energy. The ICP-OES of films deposited on alumina found that iron, manganese, and phosphorus were present in a 1:1:1 ratio. Depth profiling of the films shows homogeneity throughout the thickness of the film but gives an inconsistent atomic ratio for Fe:Mn:P of 1.28:0.72:1 (Figure<sup>2</sup>(b)). The discrepancy between the ICP results and the raw XPS data is attributed to preferential sputtering, which is well-documented in alloys or compounds containing multiple elements with different sputter yields.<sup>[58--63]</sup> For bimetallic alloys in which the sputter yield of the constituent elements is relatively constant and unaffected by composition, the following equation can be used to estimate the actual bulk composition of the material [Eq.(1)]:

$$\frac{C_{Surface}^A}{C_{Surface}^B} = \frac{C_{Bulk}^A}{C_{Bulk}^B} \frac{S^B}{S^A} \quad (1)$$

where  $C_{Surface}^A$ ,  $C_{Surface}^B$ ,  $C_{Bulk}^A$ , and  $C_{Bulk}^B$  represent the surface and bulk

concentrations of elements A and B, and  $S^A$  and  $S^B$  denote the sputter yields of the elements.<sup>[59]</sup> Using the data obtained from the XPS depth profile (Figure<sup>2</sup>) and tabulated sputter yields, the corrected ratio of Fe:Mn in the films deposited on alumina was calculated to be 1.02:1.00, which is in good agreement with the ICP-OES analysis.<sup>[60]</sup>

The individual XPS spectra of iron and phosphorus were the same for samples deposited on alumina and quartz (Figure<sup>3</sup>) and display prominent peaks at binding energies (BE) of 706.8 and 129.3 eV, respectively, which are in agreement with the binding energies reported for iron and phosphorus in  $Fe_xP$  ( $x=1, 2, \text{ or } 3$ ) phases.<sup>[64]</sup> The absence of any shoulders at higher BE's for iron and phosphorus indicate that they are either completely free from oxidation or that the relative amounts of oxidized iron and phosphorus are too small to be detectable. The XPS spectra of iron and phosphorus obtained after various sputtering times exhibited no deviation in binding energy or evidence of oxidation.

There were differences in the manganese and oxygen XPS spectra between the quartz- and alumina-deposited films. For the films deposited on quartz, there is an increase in atomic percentage of manganese approaching the quartz interface with the film, as well as fluctuations in the binding energies, indicating that the oxidation state and bonding environment of manganese is not uniform throughout the film. Representative XPS spectra of manganese obtained at several depths in the film are shown in Figure<sup>3</sup>. The peak centered around 638.7 eV corresponds well with the binding energies reported for  $Mn_xP$  ( $x=1, 2, \text{ or } 3$ ) phases, but the peak centered around 641.9 eV and the shoulder at 641.3 eV are consistent with the binding energies observed in oxidized manganese species such as MnO or  $Mn_2O_3$ .<sup>[64,65]</sup> The peak broadening and shoulders observed in the manganese  $2p_{3/2}$  spectra signify that manganese is present in both oxide and phosphide bonding environments and that the relative contribution from the oxide increases as the depth approaches the quartz. Because the XPS spectra of iron and phosphorus give no indication of oxidation, the oxygen present in the film is exclusively bound to manganese. The oxygen  $O^{1s}$  peak at 531.2 eV corresponds with a transition metal oxide. The manganese peak from the films deposited on alumina shows a sharp peak at 638.7 eV with little to no shoulder and was consistent throughout the film, thus the substrate oxidation did not occur for FeMnP on alumina.



### Morphology and phase determination

The morphologies of the films grown on the different substrates were studied using scanning electron microscopy (SEM). Films grown on quartz existed as uniform carpets of columnar, trigonal prismatic grains with an overall film thickness of  $1\text{--}3\ \mu\text{m}$  (Figure<sup>4</sup>) with triangle side lengths of approximately  $150\ \text{nm}$ . Some regions flaked off the quartz substrate under the SEM vacuum and stood on-end, allowing the film cross section to be observed directly. The trigonal crystal habit of the grains is consistent with a hexagonal cell.

Films grown on alumina exhibited a similar particle morphology (Figure<sup>5</sup>), but an apparent bimodal distribution of crystallite sizes was evident. The smaller hexagonal crystallites, similar to those on quartz, appear to grow directly on the alumina while the larger crystallites exist in spherical, micrometer sized particles, composed of the same crystalline rods, growing just above the surface. The appearance of the spheres is likely due to nucleation events dictated by the rough morphology of the underlying alumina, which prevents a more ordered array from forming.<sup>[66--68]</sup>

Powder X-ray diffraction (PXRD) experiments carried out on the decomposed  $\text{FeMn}(\text{CO})_8(\mu\text{-PH}_2)$  yielded the diffraction patterns shown in Figure<sup>6</sup>. PXRD measurements were performed on the film deposited on the quartz substrate and the films that peeled from the walls of the MOCVD and were compared to those of the bulk decomposition. Rietveld refinements were carried out by GSAS software.<sup>[31,69,70]</sup> The hexagonal  $P6_3/m$   $\text{FeMnP}$  structure from the literature was measured at  $1200^\circ\text{C}$  and was taken as the starting structure (PDF # 04-006-1275) and is shown in Figure<sup>7</sup>. Please check - was Fig 8 in submitted MS. The final Rietveld refinement shown in Figure<sup>S1</sup> (Supporting Information) yields lattice constants ( $a=b=5.923$ ,  $c=3.527\ \text{\AA}$ ) smaller than those measured at  $1200^\circ\text{C}$ ,<sup>[49]</sup> which reflects our room temperature measurement conditions. In fact, the broadening of the PXRD peaks as the angle increases is consistent with the small crystallite size of these films and it is in agreement with the small particle size observed by SEM and the stacking faults observed in the HRTEM (Figure<sup>7</sup>^b).

The PXRD pattern for the thin film on quartz has a preferred orientation along the  $(1^{\wedge}1^{\wedge}2^{\wedge}\text{Ü}\text{-}^{\wedge}1)$  plane (Figure<sup>6</sup>, top), because all of the crystallites are oriented in the same direction, which is consistent with the scanning electron microscopy data (Figure<sup>4</sup>). This PXRD pattern displays no evidence of  $\text{Mn}_x\text{O}_y$  phases, suggesting that the oxidized manganese content is very small and amorphous. Films that flaked off of the walls had no preferred orientation and broad peaks similar to those from the bulk decomposition could be observed. Subsequent experimental and analytical results combined with the previously described elemental composition suggest that the diffraction pattern observed in Figure<sup>6</sup> corresponds to hexagonal FeMnP.

In order to confirm the hexagonal phase of FeMnP, selected area electron diffraction (SAED) was recorded on a single crystal scraped from the films onto a holey-carbon film on a copper grid. The SAED pattern shown in Figure<sup>7a</sup> confirms the crystallinity of the films, and can be indexed to the hexagonal space group  $P6^{\wedge}\text{Ü}\text{-}2m$ . EDX mapping by TEM and spectrum processing also confirms the presence of FeMnP as a 1:1:1 ratio (Figure<sup>S2</sup>). The SAED pattern is consistent with the PXRD pattern (Figure<sup>6</sup>). There are extra spots and streaks in the SAED pattern that are caused by the presence of planar defects in the structure. The extra spots are from twins, and the streaks are related to stacking faults. Both types of defects are visible in the HRTEM image (Figure<sup>7b</sup> and S3 in Supporting Information)

$\text{Fe}_x\text{Mn}_{2-x}\text{P}$  prepared by conventional solid-state methods is known to be orthorhombic, with the  $\text{Co}_2\text{P}$ -type lattice, in the compositional range of  $0.65 < x < 1.35$  and hexagonal, with the  $\text{Fe}_2\text{P}$ -type lattice, outside of that range. The  $x=1$  intermetallic compound undergoes a reversible transition above  $1200^{\circ}\text{C}$  to the hexagonal  $\text{Fe}_2\text{P}$ -type lattice.<sup>[49,55]</sup> Iron, manganese, and phosphorus are known to occupy different localized 4c positions in the FeMnP orthorhombic lattice while the metal sites in the hexagonal lattice are disordered among the 3f and 3g sites and the phosphorus atoms are located in two different positions at full occupancy. In this hexagonal crystal, shown in Figure<sup>7c</sup>, the 3f site (yellow) sits inside a distorted tetrahedron whereas the 3g site sits inside a square pyramid. Since the

PXRD data suggests hexagonal FeMnP is the product upon decomposition of FeMn(CO)<sub>8</sub>(μ-PH<sub>2</sub>), it can be concluded that the decomposition process leads to occupational disorder at the metal sites preventing the ordered orthorhombic type lattice from forming. The FeMnP prepared likely retains its metastable hexagonal crystalline form because the thermal energy threshold allowing the material to recrystallize is not reached at the low temperatures employed in the film growth.

### Magnetic properties

Magnetic measurements were performed on films grown on quartz and alumina substrates. Considering a non-interacting paramagnetic particle with an angular momentum  $J$ , the molar magnetic susceptibility  $\chi \approx M/H$  is given by the Curie--Weiss law [Eq. (2)]:

$$\chi = \frac{g^2 \mu_B^2 J(J+1)}{3k_B T(T-\theta)} + \chi_0$$

where  $g$  is the Landé  $g$ -factor,  $\mu_B$  represents the Bohr magneton,  $k_B$  is the Boltzmann constant,  $\theta$  is the Weiss temperature,  $T$  is the temperature, and  $\chi_0$  is the temperature independent susceptibility.<sup>[71]</sup> Figure 8a (inset) shows the magnetic susceptibility data for quartz or alumina grown sample, measured both on zero-field cooling (yellow) and field-cooling (blue), with the inverse susceptibility ( $1/\chi$ ) displayed in the main panel. A Curie--Weiss fit of the inverse susceptibility (solid line, Figure 8a) yields a value for  $\theta$  of 131 K, an effective moment  $\mu_{\text{eff}} = g \sqrt{J(J+1)} \mu_B = 3.68 \mu_B$  per formula unit of FeMnP, and  $\chi_0 = 2.05 \times 10^{-4} \text{ emu mol}^{-1}$ . Because hexagonal Fe<sub>x</sub>Mn<sub>2-x</sub>P ( $x=1$ ) had not previously been prepared by conventional methods, the values of this effective moment and Weiss temperature were compared to, and interpolated from, known values for hexagonal Fe<sub>x</sub>Mn<sub>2-x</sub>P in the ranges  $x < 0.65$  and  $x > 1.35$ . The current data lies in the gap and is consistent with the previously reported data.<sup>[55]</sup> If the preferentially oxidized manganese had an effect on the stoichiometry of the film, the Weiss temperature would be expected to shift to a larger value, but instead matches the atomic range for Fe:Mn:P of 1:1:1. There was no difference in magnetic measurements between the films grown on one substrate or another.

The field-dependent magnetization data at 2 and 300 K was collected for magnetic fields ( $H$ ) up to 7 T and the field-dependent magnetization at 2 K was performed after the system was cooled to 2 K in zero field, as shown in Figure 8b. In contrast to the room temperature result, the magnetic hysteresis due to the magnetic coupling is observed across the whole range of the measured fields and the momentum cannot saturate even at 7 T indicating that the ferromagnetic coupling is localized inside widespread nanoscale domains. Nevertheless, the interaction between individual domains is paramagnetic, so magnetic hysteresis is observed and magnetic saturation cannot be achieved even in the high field. The as-described superparamagnetic behavior is commonly observed in nanoparticulate materials.<sup>[72]</sup> As the temperature increases, the thermal fluctuation destroys the coupling inside the small domains and the material becomes purely paramagnetic, which is shown in the 300 K measurement (Figure 8b). No hysteresis is observed at 300 K, but a small hysteresis is visible for the low temperature data. In addition, the zero-field-cooled (ZFC) and field-cooled (FC) susceptibility data in Figure 8a show a bifurcation below 100 K due to the formation of the superparamagnetic domain. The temperature-dependent measurement reveals the existence of a blocking temperature due to superparamagnetic nanoparticles observed by SEM images (Figures 4 and 5) or due to the stacking faults observed in the HRTEM images (Figure 7b).

## Conclusion

The compound  $\text{FeMn}(\text{CO})_8(\mu\text{-PH}_2)$  has proven to be a suitable precursor for the deposition of films containing Fe, Mn, and P in a 1:1:1 stoichiometric ratio present as a metastable, hexagonal phase of FeMnP. Powder X-ray diffraction patterns of the thin films confirm the hexagonal crystalline FeMnP films. XPS data obtained from depth profiling experiments indicate that quartz is a non-innocent substrate and selectively oxidizes manganese in the films. Alumina substrates were found to be a better choice for the deposition of FeMnP resulting in more homogeneous thin films. With a positive Weiss temperature of 131 K and an effective moment of  $3.68 \mu_B$ , the predicted magnetic properties have now been confirmed.<sup>[55]</sup> In addition to the ferromagnetic nature, the films on

quartz and alumina are noted to be superparamagnetic, which can be attributed to the nanoscale domains. The broad peaks observed in the powder pattern corroborate the nanosized crystallites observed on the surface by SEM imaging. PXRD and single-crystal SAED confirm the hexagonal phase of FeMnP, which has only previously been prepared by heating orthorhombic FeMnP, the more stable phase obtained by conventional solid-state methods, to over 1200<sup>°</sup>C with reversion to the orthorhombic form upon cooling. Thus, the decomposition of a molecular single-source precursor with a fixed heavy atom stoichiometry can yield thin films of difficult-to-obtain, metastable phases. The ability to coat different substrates with a bimetallic TMP is continually being studied by our group. Devices made from TMPs on electrode/semiconductor materials are being studied for catalyzing the water splitting reactions, which will be reported in a future publication.

### Acknowledgements

The authors thank Rice University, the National Science Foundation (CHE-0719369), and the Robert A. Welch Foundation (C-0976) for funding. This material is based upon work supported by the National Science Foundation Graduate Research Fellowship under Grant No. 1450681.

### Conflict of interest

The authors declare no conflict of interest.

<lit1><jnl>V.<sup>^</sup>A. Chernenko, L. Wee, P.<sup>^</sup>G. McCormick, R. Street, *J. Appl. Phys.* **1999**, 85, 7833--7837</jnl>.

<lit2><jnl>O. Tegus, E. Brück, L. Zhang, Dagula, K.<sup>^</sup>H.<sup>^</sup>J. Buschow, F.<sup>^</sup>R. De<sup>^</sup>Boer, *Phys. B* **2002**, 319, 174--192</jnl>.

<lit3><jnl>E.<sup>^</sup>J. Lisher, C. Wilkinson, T. Ericsson, L. Haggstrom, L. Lundgren, R. Wappling, *J. Phys. C* **1974**, 7, 1344--1352</jnl>.

<lit4><jnl>R.<sup>^</sup>J. Gambino, T.<sup>^</sup>R. McGuire, Y. Nakamura, *J. Appl. Phys.* **1967**, 38, 1253--1255</jnl>.

- <lit5><jnl>D. Li, H. Baydoun, C.<sup>^</sup>N. Verani, S.<sup>^</sup>L. Brock, *J. Am. Chem. Soc.* **2016**, *138*, 4006--4009</jnl>.
- <lit6><jnl>J.<sup>^</sup>F. Callejas, J.<sup>^</sup>M. McEnaney, C.<sup>^</sup>G. Read, J.<sup>^</sup>C. Crompton, A.<sup>^</sup>J. Biacchi, E.<sup>^</sup>J. Popczun, T.<sup>^</sup>R. Gordon, N.<sup>^</sup>S. Lewis, R.<sup>^</sup>E. Schaak, *ACS Nano* **2014**, *8*, 11101--11107</jnl>.
- <lit7><jnl>C.<sup>^</sup>G. Read, J.<sup>^</sup>F. Callejas, C.<sup>^</sup>F. Holder, R.<sup>^</sup>E. Schaak, *ACS Appl. Mater. Interfaces* **2016**, *8*, 12798--12803</jnl>.
- <lit8><jnl>Z. Pu, Q. Liu, A.<sup>^</sup>M. Asiri, X. Sun, *ACS Appl. Mater. Interfaces* **2014**, *6*, 21874--21879</jnl>.
- <lit9><jnl>C.-C. Hou, Q.-Q. Chen, C.-J. Wang, F. Liang, Z. Lin, W.-F. Fu, Y. Chen, *ACS Appl. Mater. Interfaces* **2016**, *8*, 23037--23048</jnl>.
- <lit10><jnl>J. Tian, Q. Liu, Y. Liang, Z. Xing, A.<sup>^</sup>M. Asiri, X. Sun, *ACS Appl. Mater. Interfaces* **2014**, *6*, 20579--20584</jnl>.
- <lit11><jnl>Y.<sup>^</sup>P. Zhu, Y.<sup>^</sup>P. Liu, T.<sup>^</sup>Z. Ren, Z.<sup>^</sup>Y. Yuan, *Adv. Funct. Mater.* **2015**, *25*, 7337--7347</jnl>.
- <lit12><jnl>Z. Xing, Q. Liu, A.<sup>^</sup>M. Asiri, X. Sun, *Adv. Mater.* **2014**, *26*, 5702--5707</jnl>.
- <lit13><jnl>Z. Zhang, B. Lu, J. Hao, W. Yang, J. Tang, *Chem. Commun.* **2014**, *50*, 11554--11557</jnl>.
- <lit14><jnl>C.<sup>^</sup>Y. Son, I.<sup>^</sup>H. Kwak, Y.<sup>^</sup>R. Lim, J. Park, *Chem. Commun.* **2016**, *52*, 2819--2822</jnl>.
- <lit15><jnl>S.<sup>^</sup>E. Habas, F.<sup>^</sup>G. Baddour, D.<sup>^</sup>A. Ruddy, C.<sup>^</sup>P. Nash, J. Wang, M. Pan, J.<sup>^</sup>E. Hensley, J.<sup>^</sup>A. Schaidle, *Chem. Mater.* **2015**, *27*, 7580--7592</jnl>.
- <lit16><jnl>E.<sup>^</sup>J. Popczun, J.<sup>^</sup>R. McKone, C.<sup>^</sup>G. Read, A.<sup>^</sup>J. Biacchi, A.<sup>^</sup>M. Wiltrout, N.<sup>^</sup>S. Lewis, R.<sup>^</sup>E. Schaak, *J. Am. Chem. Soc.* **2013**, *135*, 9267--9270</jnl>.
- <lit17><jnl>P. Jiang, Q. Liu, X. Sun, *Nanoscale* **2014**, *6*, 13440--13445</jnl>.
- <lit18><jnl>S.<sup>^</sup>L. Brock, K. Senevirathne, *J. Solid State Chem.* **2008**, *181*, 1552--1559</jnl>.

- <lit19><jnl>J. Shin, A. Waheed, K. Agapiou, W.<sup>^</sup>A. Winkenwerder, H. Kim, R.<sup>^</sup>A. Jones, G.<sup>^</sup>S. Hwang, J.<sup>^</sup>G. Ekerdt, *J. Am. Chem. Soc.* **2006**, *128*, 16510--16511</jnl>.
- <lit20><jnl>A.<sup>^</sup>N. Gleizes, *Chem. Vap. Deposition* **2000**, *6*, 155--173</jnl>.
- <lit21><jnl>C.<sup>^</sup>S. Blackman, C.<sup>^</sup>J. Carmalt, T.<sup>^</sup>D. Manning, S.<sup>^</sup>A. O'Neill, I.<sup>^</sup>P. Parkin, L. Apostolico, K.<sup>^</sup>C. Molloy, *Chem. Vap. Deposition* **2003**, *9*, 10--13</jnl>.
- <lit22><jnl>A. Panneerselvam, M.<sup>^</sup>A. Malik, M. Afzaal, P. O'Brien, M. Helliwell, *J. Am. Chem. Soc.* **2008**, *130*, 2420--2421</jnl>.
- <lit23><jnl>D.-H. Ha, L.<sup>^</sup>M. Moreau, C.<sup>^</sup>R. Bealing, H. Zhang, R.<sup>^</sup>G. Hennig, R.<sup>^</sup>D. Robinson, *J. Mater. Chem.* **2011**, *21*, 11498--11510</jnl>.
- <lit24><jnl>H. Zhang, D.<sup>^</sup>H. Ha, R. Hovden, L.<sup>^</sup>F. Kourkoutis, R.<sup>^</sup>D. Robinson, *Nano Lett.* **2011**, *11*, 188--197</jnl>.
- <lit25><jnl>J. Kibsgaard, C. Tsai, K. Chan, J.<sup>^</sup>D. Benck, J.<sup>^</sup>K. Nørskov, F. Abild-Pedersen, T.<sup>^</sup>F. Jaramillo, *Energy Environ. Sci.* **2015**, *8*, 3022--3029</jnl>.
- <lit26><jnl>K. Senevirathne, R. Tackett, P.<sup>^</sup>R. Kharel, G. Lawes, K. Somaskandan, S.<sup>^</sup>L. Brock, *ACS Nano* **2009**, *3*, 1129--1138</jnl>.
- <lit27><jnl>K. Senevirathne, A.<sup>^</sup>W. Burns, M.<sup>^</sup>E. Bussell, S.<sup>^</sup>L. Brock, *Adv. Funct. Mater.* **2007**, *17*, 3933--3939</jnl>.
- <lit28><jnl>J. Park, B. Koo, K.<sup>^</sup>Y. Yoon, Y. Hwang, M. Kang, J.<sup>^</sup>G. Park, T. Hyeon, *J. Am. Chem. Soc.* **2005**, *127*, 8433--8440</jnl>.
- <lit29><jnl>K.<sup>^</sup>Y. Yoon, Y. Jang, J. Park, Y. Hwang, B. Koo, J.<sup>^</sup>G. Park, T. Hyeon, *J. Solid State Chem.* **2008**, *181*, 1609--1613</jnl>.
- <lit30><jnl>E. Ye, S.<sup>^</sup>Y. Zhang, S.<sup>^</sup>H. Lim, M. Bosman, Z. Zhang, K.<sup>^</sup>Y. Win, M.<sup>^</sup>Y. Han, *Chem. Eur. J.* **2011**, *17*, 5982--5988</jnl>.
- <lit31><jnl>A.<sup>^</sup>C. Colson, K.<sup>^</sup>H. Whitmire, *Chem. Mater.* **2011**, *23*, 3731--3739</jnl>.
- <lit32><jnl>S.<sup>^</sup>E.<sup>^</sup>R. Hiscocks, J.<sup>^</sup>B. Mullin, *J. Mater. Sci.* **1969**, *4*, 962--973</jnl>.

- <lit33><jnl>C.<sup>^</sup>S. Blackman, C.<sup>^</sup>J. Carmalt, S.<sup>^</sup>A. O'Neill, I.<sup>^</sup>P. Parkin, L. Apostolico, K.<sup>^</sup>C. Molloy, *Chem. Mater.* **2004**, *16*, 1120--1125</jnl>.
- <lit34><jnl>C.<sup>^</sup>S. Blackman, C.<sup>^</sup>J. Carmalt, S.<sup>^</sup>A. O'Neill, I.<sup>^</sup>P. Parkin, K.<sup>^</sup>C. Molloy, L. Apostolico, *J. Mater. Chem.* **2003**, *13*, 1930--1935</jnl>.
- <lit35><jnl>S. Motojima, T. Wakamatsu, K. Sugiyama, *J. Less-Common Met.* **1981**, *82*, 379--383</jnl>.
- <lit36><jnl>I.<sup>^</sup>M. Watson, J.<sup>^</sup>A. Connor, R. Whyman, *Thin Solid Films* **1991**, *196*, L21--L24</jnl>.
- <lit37><jnl>C.<sup>^</sup>S. Blackman, C.<sup>^</sup>J. Carmalt, T.<sup>^</sup>D. Manning, I.<sup>^</sup>P. Parkin, L. Apostolico, K.<sup>^</sup>C. Molloy, *Appl. Surf. Sci.* **2004**, *233*, 24--28</jnl>.
- <lit38><jnl>J.<sup>^</sup>T. Scheper, K.<sup>^</sup>C. Jayaratne, L.<sup>^</sup>M. Liable-Sands, G.<sup>^</sup>P. Yap, A.<sup>^</sup>L. Rheingold, C.<sup>^</sup>H. Winter, *Inorg. Chem.* **1999**, *38*, 4354--4360</jnl>.
- <lit39><jnl>T. Thomas, C.<sup>^</sup>S. Blackman, I.<sup>^</sup>P. Parkin, C.<sup>^</sup>J. Carmalt, *Eur. J. Inorg. Chem.* **2010**, 5629--5634</jnl>.
- <lit40><jnl>R.<sup>^</sup>G. Palgrave, I.<sup>^</sup>P. Parkin, *New J. Chem.* **2006**, *30*, 505--514</jnl>.
- <lit41><jnl>T.<sup>^</sup>S. Lewkebandara, C.<sup>^</sup>H. Winter, *Chem. Vap. Deposition* **1996**, *2*, 75--77</jnl>.
- <lit42><jnl>J. Choi, S. Choi, M.<sup>^</sup>H. Sohn, H. Park, Y. Park, H.-M. Park, S.<sup>^</sup>C. Hong, S. Cho, *J. Magn. Magn. Mater.* **2006**, *304*, e112--e114</jnl>.
- <lit43><jnl>P.<sup>^</sup>J. Walsh, N. Bottka, *J. Electrochem. Soc.* **1984**, *131*, 444--446</jnl>.
- <lit44><jnl>A. Panneerselvam, C.<sup>^</sup>Q. Nguyen, J. Waters, M.<sup>^</sup>A. Malik, P. O'Brien, J. Raftery, M. Helliwell, *Dalton Trans.* **2008**, 4499--4506</jnl>.
- <lit45><jnl>F.-R. Klingan, A. Miehr, R.<sup>^</sup>A. Fischer, W.<sup>^</sup>A. Herrmann, *Appl. Phys. Lett.* **1995**, *67*, 822--824</jnl>.
- <lit46><jnl>M. Solzi, C. Pernechele, M. Ghidini, M. Natali, M. Bolzan, *J. Magn. Magn. Mater.* **2010**, *322*, 1565--1568</jnl>.



- <lit47><jnl>A.<sup>^</sup>C. Colson, C.<sup>^</sup>W. Chen, E. Morosan, K.<sup>^</sup>H. Whitmire, *Adv. Funct. Mater.* **2012**, *22*, 1850--1855</jnl>.
- <lit48><jnl>A.<sup>^</sup>P. Leitner, J.-H. Chen, D.<sup>^</sup>E. Schipper, K.<sup>^</sup>H. Whitmire, *Chem. Mater.* **2016**, *28*, 7066--7071</jnl>.
- <lit49><jnl>B. Chenevier, J.<sup>^</sup>L. Soubeyroux, M. Bacmann, D. Fruchart, R. Fruchart, *Solid State Commun.* **1987**, *64*, 57--61</jnl>.
- <lit50><jnl>E. Brück, *J. Phys. D. Appl. Phys.* **2005**, *38*, R381--R391</jnl>.
- <lit51><jnl>H. Kobayashi, J. Umemura, X.-W. Zhan, Y. Ohishi, Y. Uwatoko, H. Fujii, N. Sakai, *J. Phys. Soc. Japan* **2011**, *80*, 084719</jnl>.
- <lit52><jnl>L. Caron, M. Hudl, V. Höglin, N.<sup>^</sup>H. Dung, C.<sup>^</sup>P. Gomez, M. Sahlberg, E. Brück, Y. Andersson, P. Nordblad, *Phys. Rev. B* **2013**, *88*, 094440</jnl>.
- <lit53><jnl>Z. Gercsi, E.<sup>^</sup>K. Delczeg-Czirjak, L. Vitos, A.<sup>^</sup>S. Wills, A. Daoud-Aladine, K.<sup>^</sup>G. Sandeman, *Phys. Rev. B* **2013**, *88*, 024417</jnl>.
- <lit54><jnl>X.<sup>^</sup>B. Liu, J. Ping<sup>^</sup>Liu, Q. Zhang, Z. Altounian, *Phys. Lett. A* **2013**, *377*, 731--735</jnl>.
- <lit55><jnl>S. Nagase, H. Watanabe, T. Shinohara, *J. Phys. Soc. Japan* **1973**, *34*, 908--910</jnl>.
- <lit56><jnl>A.<sup>^</sup>C. Colson, K.<sup>^</sup>H. Whitmire, *Organometallics* **2010**, *29*, 4611--4618</jnl>.
- <lit57><jnl>B.<sup>^</sup>J. Tan, K.<sup>^</sup>J. Klabunde, T. Tanaka, H. Kanai, S. Yoshida, *J. Am. Chem. Soc.* **1988**, *110*, 5951--5958</jnl>.
- <lit58><jnl>P.<sup>^</sup>S. Ho, J.<sup>^</sup>E. Lewis, H.<sup>^</sup>S. Wildman, J.<sup>^</sup>K. Howard, *Surf. Sci.* **1976**, *57*, 393--405</jnl>.
- <lit59><jnl>S. Hofmann, *Surf. Interface Anal.* **1980**, *2*, 148--160</jnl>.
- <lit60><jnl>J. Mahan, A. Vantomme, *Phys. Rev. B* **2000**, *61*, 8516--8525</jnl>.
- <lit61><jnl>S. Hofmann, *Rep. Prog. Phys.* **1998**, *61*, 827--888</jnl>.
- <lit62><jnl>H.<sup>^</sup>W. Werner, N. Warmoltz, *Surf. Sci.* **1976**, *57*, 706--714</jnl>.

- <lit63><jnl>J. Coburn, *J. Vac. Sci. Technol.* **1976**, *13*, 1037</jnl>.
- <lit64><jnl>P.<sup>^</sup>E.<sup>^</sup>R. Blanchard, A.<sup>^</sup>P. Grosvenor, R.<sup>^</sup>G. Cavell, A. Mar, *Chem. Mater.* **2008**, *20*, 7081--7088</jnl>.
- <lit65><jnl>J.<sup>^</sup>C. Carver, G.<sup>^</sup>K. Schweitzer, T.<sup>^</sup>A. Carlson, *J. Chem. Phys.* **1972**, *57*, 973</jnl>.
- <lit66><jnl>N.<sup>^</sup>V. Tarakina, S. Schreyeck, M. Luysberg, S. Grauer, C. Schumacher, G. Karczewski, K. Brunner, C. Gould, H. Buhmann, R.<sup>^</sup>E. Dunin-Borkowski, *Adv. Mater. Interfaces* **2014**, *1*, 1400134</jnl>.
- <lit67><jnl>M. Strafela, H. Leiste, K. Seemann, H.<sup>^</sup>J. Seifert, S. Ulrich, *Vacuum* **2016**, *131*, 240--245</jnl>.
- <lit68><jnl>A. Jara, B. Fraisse, V. Flaud, N. Fréty, G. Gonzalez, *Surf. Coat. Technol.* **2017**, *309*, 887--896</jnl>.
- <lit69><other>A.<sup>^</sup>C. Larson, R.<sup>^</sup>B. Von<sup>^</sup>Dreele, *General Structure Analysis System (GSAS)*, Los Alamos National Laboratory Report LAUR 86-748 **2004**</other>.
- <lit70><jnl>B.<sup>^</sup>H. Toby, *J. Appl. Crystallogr.* **2001**, *34*, 210--213</jnl>.
- <lit71><book>C. Kittel, *Introduction to Solid State Physics*, Wiley, **2004**</book>.
- <lit72><jnl>S. Bedanta, W. Kleemann, *J. Phys. D* **2009**, *42*, 013001</jnl>.

Received: January 13, 2017

Accepted Article published: December 30, 1899

Published online: <?><?>

- Figure<sup>^</sup>1 Schematic diagram of the home-built MOCVD apparatus.
- Figure<sup>^</sup>2 XPS depth profile of FeMnP deposited on a)<sup>^</sup>quartz and b)<sup>^</sup>alumina.
- Figure<sup>^</sup>3 XPS spectra of FeMnP thin films. The binding energies for Fe and P remain unchanged during depth profiling and show no evidence of oxidation. The binding energies for Mn and O change during depth profiling and show evidence of film oxidation by the quartz substrate. Spectra from the film deposited on alumina shown in black; the film

deposited on quartz is shown at two different depths, yellow in the middle and red near the substrate.

Figure<sup>4</sup> FeMnP film grown on quartz from  $\text{FeMn}(\text{CO})_8(\mu\text{-PH}_2)$  showing a) a flake of film sitting on edge atop pristine film, b) trigonal grain features, and c) uniformity of the film.

Figure<sup>5</sup> SEM micrographs at a) lower magnification and b) higher magnification of FeMnP grown on alumina.

Figure<sup>6</sup> Powder X-ray diffraction patterns of the deposited film on quartz (green), the film that flaked from the walls of the MOCVD (blue), the solventless decomposition of  $\text{FeMn}(\text{CO})_8(\mu\text{-PH}_2)$  (violet), and the pattern for hexagonal FeMnP measured at  $1200^\circ\text{C}$  (PDF # 04-006-1275) (orange).<sup>[49]</sup>

Figure<sup>7</sup> a) Single crystal SAED pattern for hexagonal  $P6_3/m$  FeMnP scraped from the film grown on alumina. b) HRTEM images of the crystalline rod from the film grown on alumina. Planar defects (twins and stacking faults) are present in the structure. c) The hexagonal  $P6_3/m$  FeMnP crystal structure is shown in the polyhedral view. The metal atoms are randomly distributed in 3f (yellow) and 3g (purple) sites as described in the text.

Figure<sup>8</sup> Magnetization measurements were performed on the films grown on quartz and alumina as a function of a) temperature (zero-field-cooled [ZFC] and field-cooled [FC]) and b) magnetic field. The hysteresis at low temperatures illustrates the typical superparamagnetic behavior as described in the text. Is the plotted data from the quartz or alumina substrate?